This is a repository copy of *An alternative admixture to reduce sorptivity of alkali-activated slag cement by optimising pore structure and introducing hydrophobic film*.

White Rose Research Online URL for this paper:
http://eprints.whiterose.ac.uk/139792/

Version: Accepted Version

An alternative admixture to reduce sorptivity of alkali-activated slag cement by optimising pore structure and introducing hydrophobic film

Qing Li[a], Kai Yang[a, b*], Changhui Yang[a*]

a: College of Materials Science and Engineering, Chongqing University, China, 400045
b: School of Civil Engineering, University of Leeds, Leeds, UK, LS2 9JT

Abstract: The high water absorption rate of alkali-activated slag (AAS) cement, which causes concerns to designers and constructors as "long-term" durability comes into question, was addressed using an alternative admixture, calcium stearate (CaSt). The macro- and micro- performance of AAS cement with two levels of CaSt dosage (4 wt%, 8 wt% of slag) were characterised under the water to binder ratio (W/B) ranging from 0.35 to 0.45 and benchmarked against corresponding Portland cement (PC) samples by sorptivity along with compressive strength, porosity, electrical resistivity, pore connectivity, pore size distribution and pore geometries. The interpretation of results showed that CaSt played an instrumental role in pore structure features of AAS and the use of CaSt could significantly reduce its sorptivity, even lower than the corresponding PC samples. It is also found that the recommended usage of CaSt is 4% of slag, beyond which no significant variation in sorptivity can be detected. The performance improvement was caused by two main mechanisms, optimising the pore structure (more entrained pores, less pore connectivity factor and less microcracks) and introduce of the hydrophobic film on the pore surface. One limitation of using CaSt was noted as well. That is, the strength development of AAS can be affected and it can be avoided through modifying mix proportions according to practical requirements. Therefore, CaSt can be used as a chemical admixture for AAS to solve the concern on its high sorptivity behaviour.

Key words: alkali activated slag cement; sorptivity; calcium stearate; pore structure; hydrophobic film

1. Introduction

Ground granulated blast-furnace slag (GGBFS) is a by-product of iron industry. In 2017, China iron industry produced 300 million tons of GGBFS and only 40~50% was used in the construction sector [1]. Due to its amorphous nature, GGBFS has a great success as supplementary cementitious material used in conventional Portland cement (PC) system to improve overall performance of concrete [2]. Another approach to utilise GGBFS is to chemically activate using different metal salts and lime, generally named as alkali activation [3]. Alkali-activated slag (AAS) cement is a clinker free binder and previous studies confirmed that it can offer a range of high performance surpassing PC, e.g. high strength development [4], high resistance against chemical attacks [5, 6], high resistance against chloride ingress [7, 8]. Meanwhile, AAS cement consumes less energy, less raw materials and is considered as one type of "high-performance" cement [9]. It is important to emphasise that AAS cements must not be considered as a simple replacement for PC in all types of concrete; instead, they enlarge the assortment of binders and thus, make possible a better choice of concrete, slurry or mortar of the desired properties.

Despite a great potential, industry application of AAS is still limited and most works are restricted to research activities in laboratory. Recently, the first structural use of site cast AAS concrete was completed in China [10], in which its general performance (workability, strength development) and relevant construction procedures were established and basic rules were written in the industrial standard –DBJ50/T-205-2014 [11]. In order to further explore practical uses of AAS, several technical limitations, e.g. high shrinkage, potential durability related issues, need to be addressed carefully. Among them, durability is fundamental performance and is a constant source of concern that requires a careful investigation. This is reasonable, since Portland cement (PC) concretes have been well-known for nearly 200 years, while the first experience with AAS concrete on an industrial scale was acquired as late as six decades ago. Although AAS has hydration products close to that in ancient motors and small pores, numerous studies have shown questionable results over its durability and hence, it is useful to judge, understand and optimise the long-term durability performance of AAS.

Anyone associated with the concrete industry and confronted by durability assessment has periodically used the water sorptivity. This parameter is calculated according to the unsaturated flow theory so as to give some indication of ingress rates of aggressive chemicals and liquids to structural concrete. Numerous researchers from different institutions, including Collins and Sanjayan [12], Bernal et al. [8], Law et al. [13,14], have reported that the sorptivity of AAS is higher than that of PC for a given W/B ratio. In authors' previous study [15], similar results were obtained as well. The high sorptivity of AAS can be attributed to two main reasons. The first one is the high pore connectivity of AAS, which results from micro-cracks in the matrix and large proportion of fine pores [16]. The second reason is the formation of superfluous dry salts in the drying process [17], which can absorb a large amount of moisture during the sorptivity measurement.

In order to reduce water sorptivity of AAS, a range of techniques have been applied, e.g. changing mix designs and curing conditions [18], adding inert mineral admixtures [19], adding steel fiber [20]. Using these techniques can decrease the water transport rates of AAS, while the sorptivity is still higher than that of the corresponding PC specimens. As such, the water transport of AAS is still too high and further works are needed. Ge [21], He [22] and Maryoto [23] highlighted that adding calcium stearate (CaSt) into the PC system can remarkably reduce absorption rates due to formation of hydrophobic films on the surface of hydration products.

Inspired by possibilities of obtaining analogous results in AAS, this study was designed to investigate influence of CaSt on water sorptivity of AAS. Meanwhile, electrical responses (bulk conductivity, pore solution conductivity), compressive strength, pore structure (mercury intrusion porosimetry, scanning electron microscope, porosity) of PC and AAS with and without CaSt were also examined to reveal its working mechanisms.

2. Experimental programme

2.1 Raw materials

Ground granulated blast furnace slag (GGBFS) provided by Chongqing Iron and Steel Company was ground in a ball mill for 30 minutes, and then placed to a vibration mill for another 20-minute grounding. After this, the specific area and density of GGBFS were measured and its Blaine fineness and density were 505 m^2/kg and 2.95 g/cm^3. Ordinary Portland cement (CEM I: Blaine fineness: 350 m^2/kg, density: 3.15 g/cm^3) confirming to the Chinese National Standard GB175-2007 [24] was used to prepare the PC samples for comparison. **Table 1** summarises the chemical compositions of the GGBFS and Portland cement (PC) used in this study.

The AAS binders were manufactured at the activator (Na_2O) concentration of 5 wt.% of GGBFS. The alkaline activator was a liquid sodium silicate (water glass) with a modulus (SiO_2/Na_2O molar ratio) of 1.5. It was prepared by mixing the NaOH solution and commercial sodium silicate (modulus: 2.6) in the pre-calculated ratio. In order to avoid potential influences of dissolution heat on experimental results, the alkaline solution was cooled at a constant temperature of 20 ($\pm$1) ^{o}C for 2 hours prior to mixing AAS mixture.

Calcium stearate (CaSt) with a density of 1.08 g/cm^3, produced by Chengdu Kelong chemical reagent factory, was used as the admixture to improve the permeation performance of AAS cement.

2.2 Sample preparation and curing regime

Table 2 gives the AAS and PC mix proportions used in this study. Paste specimens prepared included $40 \times 40 \times 40$ mm^3 cubes and Φ 40 mm $\times$ 100 mm cylinders. After mixing, specimens were compacted on a vibration table until no air bubbles appeared on the surface and then, they were covered with thick polythene sheets to prevent moisture loss. All specimens were de-moulded after 1 day and were moved into a standard curing room (20 ($\pm$2) ^{o}C, RH > 95%) until testing. The cubic specimens were used to measure the bulk electrical conductivity, water sorptivity and compressive strength. The cylindrical specimens were used to extract the pore solution for conductivity measurements, porosity and microstructure analysis.

2.3 Test procedures

2.3.1 Compressive strength

Compressive strength of AAS cement samples was determined according to the Chinese National Standard GB/T17671-1999 [25] at the age of 3, 7, 14 and 28 days. All the results of compressive strength reported are the average value of 3 specimens.

2.3.2 Porosity

1) Total porosity

The total porosity was estimated through measurements of the density of the bulk specimen, including closed and connected pores. The density of the paste specimen was measured according to the Chinese National Standard GB/T 208-2014[26]. At the age of 28 days, paste samples were crushed and grounded and passed through the square hole sieve (0.90 mm), after which the pastes powders were dried in an oven at a temperature of 110 ($\pm$5) °C for 2 hours. The mass of the samples were measured as m_0 (accurate to 0.01g) and their volume (V) was determined using a Le Chatelier Flask. The pastes density, ρ_P (g/cm^3), can be calculated according to the following Equation (1):

$$\rho_P = \frac{m_0}{V} \tag{1}$$

The total porosity of the sample was determined according ASTM C462 [27]. The paste samples were saturated by immersing into a water tank at 20 °C and the mass of the surface dried specimen was measured after 48-hour immersion. The surface moisture was removed by a towel, and the mass was

determined. Then, the specimen was suspended by a wire and its apparent mass in water was determined, m_{sus} (g). After this, the paste samples were dried in an oven at a temperature of 110 (±5) °C for 24 h, and were placed in a desiccator at a room temperature, so the mass, m_{dry} (g), was determined. The total porosity can be determined according to the following Equation (2):

$$\phi_{T} = \frac{(m_{imm} - m_{sus}) - \dfrac{m_{dry}}{\rho_{P}}}{m_{imm} - m_{sus}}$$ (2)

where ϕ_{T} denotes the total porosity (%); m_{imm} denotes the mass of the surface-dried the specimen (g).

2) Connected porosity

The connected porosity was assessed by measuring accessible porosity. At the age of 28 days, paste samples were crushed to particle sizes of around 10 mm and immersed in a solution of pure ethanol for 3 days to stop further hydration. Samples were then dried in a 40 °C vacuum oven and the mass recorded as $M_{40°C}^{0}$ (g). The vacuum was applied in the drying process to avoid the problem of carbonation which could block the pores and affect final results. The vacuum pressure was around 40 mm Hg that would not destroy hydration products, e.g. ettringite [28]. Oven dried samples were saturated by immersing in deionised water for 24 hours, after which the saturated surface dry mass was recorded as M_{S} (g). The volume of crushed samples was determined by the Le Chatelier Flask's [29]. The porosity was then computed according to the following equation:

$$\phi_{C} = \frac{M_{S} - M_{40°C}^{0}}{\rho_{w}v} \times 100\%$$ (3)

where ϕ_{C} is the paste capillary porosity (%); M_{S} is the mass of saturated sample (g); $M_{40°C}^{0}$ is the constant mass of samples dried at 40 °C (g); ρ_{w} is the density of water (g/cm^{3}); and v is the bulk volume of cement paste (cm^{3}).

2.3.3 Water sorptivity test

It needs to be pointed out that no drying methods have specifically been developed for AAS to date and the effect of different drying techniques on the microstructure of AAS samples is not well studied. Therefore, before carrying out the study reported in this paper, relevant standards and recommendations for sorptivity measurements were checked, including ASTM: C1585 [30], RILEM: TC-116 [31], BS-EN:13057 [32] and BS: 1881-122 [33]. In recommended procedures, the drying temperature generally varies from 40 °C to 50 °C to remove free moisture in the sample and after drying for a specific duration, the samples are placed in an air tight container for 10 days to 15 days to redistribute the moisture. Against these, the sorptivity of paste samples was determined according to the procedures described by Yang et al. [15]. The 40 mm × 40 mm × 40 mm specimens were cut into 20 mm × 20 mm × 20 mm cube by a precision cutting machine (JMQ-60Z) to minimise the micro-cracking caused by the preconditioning process. The preprocessed specimen was dried in an oven at 40 °C, RH = 25% for 7 days. Before carrying out tests, specimens were sealed around with aluminum foil tapes and were kept in a desiccator for 1 day to reach the room temperature. For each sample, one surface was in contact with water in a shallow tray. Water was absorbed through the bottom surface and the mass increase of the specimens was measured every minute over a period of 25 min. To calculate the value of sorptivity, the data points were fitted using linear regression as shown in Equation (4):

$$i = a + St^{0.5}$$ (4)

where i is the volume of water absorbed per unit area (mm^3/mm^2); S is a material constant called the sorptivity (mm/min$^{0.5}$); a is a constant (mm) and t is the time elapsed (min).

2.3.4 Bulk electrical conductivity
The resistivity of paste samples was measured by a two-point uniaxial method with an LCR bridge [28]. Moisture on the sample surface was removed by a dry towel before measurements. Samples were placed between two thin parallel metal plates and in order to achieve an effective contact moist sponge was placed between the metal plate and the specimen. Alternating current (AC) with a frequency of 1 kHz was applied to reduce the effect of polarisation and the whole testing process lasted for less than 2 min. As such, any variation in the moisture content of the sponge during measurements could be minimised. The impedance from the measurements was converted to resistance, from which the electrical resistivity was calculated using Equation (5):

$$\sigma = R\frac{A}{l} \qquad\qquad (5)$$

where σ is the electrical resistivity ($\Omega \cdot$m); R is the resistance of a uniform specimen (Ω); A is the cross-section area of a specimen (m^2); l is the length of the specimen (m). These values were then used to calculate the conductivity (S/m) of each specimen as the inverse of the electrical resistivity.

2.3.5 Pore solution analysis
The pore solution of AAS and PC paste samples was extracted under a constant pressure of 407.6 MPa (800 kN on 1962.5 mm^2) for 45 min and the electrical conductivity measured immediately using a conductivity probe (Company: INESA, DDS-11a). Further details of this method are described by Vollpracht et al. [34]and our previous study [28].

2.3.6 Mercury intrusion porosimetry (MIP)
At the age of 28d, the cube samples were crushed to particles with size of 3–5 mm to avoid additional pore volume entrapment by the size effect during MIP [35]. The samples were then tested for pore distribution using the MIP (Micromeritics Auto Pore IV 9500) with the applied maximum and minimum pressures of 414 MPa and 1.4 kPa respectively. The maximum and minimum applied pressures correspond to cylindrical pore sizes of 3 nm and 800 μm respectively. The equilibrium time for each applied pressure level was controlled to 10 seconds.

2.3.7 Scanning electron microscope
Scanning electron microscope (SEM) analysis was employed to obtain microstructure features of AAS and PC samples. Samples for SEM tests were sourced from the crushed paste specimens, which were then vacuum dried for 3 days at a constant temperature of 40 (±1) ºC and specimens were coated with gold using a sputtering device. The TESCAN VEGA 3 LMH fitted with a tungsten filament emission source was used to capture the images. Observations were undertaken at an accelerating voltage of 20 kV with a secondary electron (SE) detector [36].

2.3.8 Contacting behaviour assessment
The contacting behaviours were determined according to the procedures described by Tran et al. [37]. The 40 mm × 40 mm × 40 mm cube specimen was cut into the 5 mm × 10 mm × 20mm specimen by a diamond saw. In order to obtain a smooth surface, the test surface was polished by an automatic polish-grinding machine with an abrasive paper (2000 mesh number) for 2 mins. The polished samples were placed into a 40 ºC oven for 1 hour to remove the surface moisture. After this, a drop of water was dropped on the surface of the sample and the pictures were taken after 5 mins using an industrial camera.

3. Results and discussion

3.1 Compressive strength

Figure 1 shows the results of compressive strength of PC and AAS with different dosages of CaSt. As shown in **Figure 1**, the compressive strength of specimen grew as age increased and the W/B ratio decreased. In addition, the higher compressive strength of AAS control group than that of PC was observed, e.g. compressive strength of AAS-35-0% at 28 days is 81.5MPa, much higher than that of PC-35 (65.5MPa). These observations agree well with results reported in previous studies [15, 28].

Addition of CaSt significantly decreased the compressive strength of AAS and the ratio of reduction is proportional to its dosage. Due to very limited literatures, it is not easy to make a direct comparison between results in **Figure 1** and results from other studies. However, Jiang et al. [38] investigated the influence of CaSt on the water and chloride resistance of the PC samples. In their study, only 0.5% CaSt (mass ratio) was added in the PC concrete with the W/B ratio of 0.5 and the results indicated the compressive strength at 28 days declined 50% caused by CaSt. This associated with the strong hydrophobic effects of CaSt that can delay the hydration process of Portland cement [21, 39]. According to the results obtained in this study, CaSt has a similar impact on development of compressive strength of AAS, but AAS is much less sensitive than PC, as only 20% deceases in compressive strength were observed for AAS at 8% dosage of CaSt. The decrease of compressive strength is also due to an increase in total porosity, which will be discussed in the next section.

3.2. Porosity

Porosity is a key parameter to describe the pore structure of cement-based materials [40, 41] and two common indicators, total porosity and connected porosity, were determined to examine the influence of CaSt on porosity of AAS in this study.

3.2.1 Total porosity

The total porosity is defined as the ratio of the total empty space in porous material that is closely related to the compressive strength [42, 43]. **Table 3** gives the total porosity of AAS and PC at the age of 28 days. It can be found that when the W/B was 0.35, the total porosity of AAS control group was close to PC, while the W/B was increased to 0.45, a significant high value was observed for AAS. Here comes the condition that the water and water glass were regarded as liquid phase and slag/cement was regarded as solid phase, so the percentage of the volume of liquid phase to total volume gives the initial porosity. It was estimated that when the W/B was 0.45, the initial porosity of AAS was 63.2%, while that in PC was 54%. Thus, the initial porosity was higher in AAS than in PC, which could be one main reason why the total porosity in AAS is high for the 0.45 mix. Meanwhile, for a given Na_2O content, the hydration process for the high W/B ratio mixes is much slower due to the low alkaline concentration. This is another reason why AAS is more sensitive to the W/B [44, 45].

As shown in **Table 3**, the total porosity of AAS increased with the increasing amount of CaSt, which can explain variations of compressive strength of AAS with CaSt (given in **Figure 1**). In addition to this, the influence of CaSt relies on its dosage amount, as the total porosity of AAS mixes with 4% CaSt clumped 6-7%, and the growth of total porosity is less than 3% when 8% CaSt was added. It suggests that relatively non-significant impact would be detected on AAS, when the dosage of CaSt is beyond 4%.

3.2.2 Connected porosity

Connected porosity, or accessible porosity, controls transport properties of AAS and PC [46-48] and **Figure 2** plots the connected porosity of AAS and PC specimens at different ages. Clearly, there are no significant variations beyond 7 days for all PC and AAS samples. It has been established that as the

hydration proceeded, more solid phases were formed and pores became packed [38, 42], which resulted in reduction in the connected porosity. Furthermore, unlike the total porosity, the connected porosity values of PC and AAS with/without CaSt stay closely to each other for a given W/B ratio, suggesting that this parameter is not affected by use of CaSt. Combining the results in **Figure 2** and **Table 3** suggests that the total porosity of AAS increased after CaSt addition, while the connected porosity is not significantly affected. This means that CaSt introduced disconnected pores in AAS. This is because CaSt could entrain air in the mixture [12, 13] and form closed pores inside AAS, which can lead to an increase of the total porosity.

3.3 Water sorptivity

Figure 3 compares the water sorptivity values of PC and AAS with/without CaSt. Unsurprisingly, the water sorptivity of AAS increased with an increase of the W/B and for a given W/B, the water sorptivity of the AAS control group is much higher than the PC sample, which is in line with the research of Yang et al. [15] and Shi [43]. Encouraging results were obtained, when CaSt was added into AAS. For example, for the AAS with the W/B of 0.45 and 4% CaSt, its sorptivity value decreased about by 80%, only half of the PC sample. It means that CaSt can efficiently reduce the water sorptivity of AAS and AAS with CaSt can achieve much better performance than the PC sample. Furthermore, the use of CaSt in AAS could remove the influence of the W/B on sorptivity and beyond 4%, CaSt did not affect sorptivity of AAS significantly, suggesting that 4% would be sufficient for improving the water transport performance of AAS. Although the porosity results of CaSt added AAS samples (as shown in **Figure 2** and **Table 3**) give certain indications on reduction of sorptivity, other reasons must exist for such a distinguished improvement.

3.4 Sorptivity improvement mechanisms

3.4.1 Pore connectivity
Pore connectivity is one key factor to control the water sorptivity, but this parameter cannot be easily assessed using a direct method. In this study, two independent techniques, electrical responses and MIP, were applied to estimate the value of pore connectivity.

1) Pore connectivity determined by electrical responses
It has been well established [49-52] that the electrical responses of cement-based materials can be used to estimate their pore connectivity according to the following Equation (6):

$$\sigma = \sigma_0 \phi_{cap} \beta \tag{6}$$

where σ is the bulk conductivity of the paste sample (S), σ_0 is the conductivity of the pore solution (S); ϕ_{cap} is the volume fraction of capillary porosity (%), and β is the connectivity factor (inverse tortuosity).

The electrical responses and the calculated connectivity of PC and AAS with and without CaSt are summarised in **Figure 4**. It can be found that the pore connectivity decreased with the increase of the W/B, and the pore connectivity of the AAS control group was smaller than corresponding PC, which are consistent with results of Rodrigue et al [53]. In general, the water sorptivity of cement-based materials is closely correlated with the pore connectivity [12, 13, 53]. However, results given in **Figure 3** and other studies [7, 15, 53] indicated that for a given W/B ratio, the water sorptivity of AAS is high in comparison to the PC. This could be caused by the preconditioning regime to remove the moisture that might cause additional changes in microstructure of AAS, because this material is more sensitive to the moisture loss [54, 55]. In addition to this, AAS has more salts in the pore system [17, 56] and these salts have strong water absorption capabilities [57] that can increase its water absorption

rates as well. Furthermore, the driving force of water ingress is greater in AAS than that in PC due to the up-taken water accompanying by dissolving salts and high proportion of fine pores in AAS. As such, its water sorptivity of AAS may not behave as well as its low pore connectivity factor.

The most interesting feature in **Figure 4** is a significant decrease of pore connectivity, when CaSt was added. For example, the pore connectivity of AAS with 8% CaSt decreases by 35% (W/B: 0.45) and 22% (W/B: 0.35) compared with the control AAS group. It suggests that CaSt was more effective for the high W/B AAS mixture. This is because when CaSt can introduce the closed pores (as shown in **Figure 2** and **Table 3**) that could block the capillaries, hence reducing the pore connectivity.

2) Pore connectivity determined by MIP

Due to the "ink-bottle" shape pores, the size from MIP is actually the size of "pore neck" that connects larger pores. However, other researchers stated that acceptable estimation of pore structure can be obtained from MIP data through strict experimental control and proper interpretation [58-60]. In this paper, data from MIP were used to assess two characteristics of microstructure, pore size distribution of PC and AAS with/without CaSt and pore connectivity.

a) Pore size distribution

The results of pore size distribution of PC and AAS with and without CaSt are shown in **Figure 5**. The porosity estimated from MIP measurements may be closer to the total porosity, since mercury pressures can collapse small pores or break through to isolated pores [9-11, 15, 61]. It can be found that when the W/B is 0.45, the porosity of AAS control group obtained from MIP is close to PC. Comparing to the control group (AAS-45-0, 18.5%), the AAS-45-4% and the AAS-45-8% groups had relatively high porosity values, i.e. 32.4% and 35.8%. The higher porosity obtained from MIP measurements agrees with the total porosity (shown in **Table 3**). From the data represented in **Figure 5-(b)** and **Table 4**, the pores in AAS became coarse after using the CaSt. According to results of Collins et al. [62], the high porosity of pores within the mesopore region (10-20 nm) in AAS is one main driving force for its high shrinkage, which contributed to a great cracking tendency [63]. Use of CaSt in AAS can introduce more ink-bottle pores to change the pore size distribution and may reduce the capillary tension, thus control potential variations in microstructure during the drying process and reduce improve the water sorptivity.

b) Pore connectivity

According to Zeng et al. [64], the pore connectivity of AAS can be calculated by the pore entrapment obtained from the MIP mercury intrusion and extrusion. In order to calculate the pore entrapment, a factor, α_θ, is defined to quantify the contact angle hysteresis:

$$\alpha_\theta = \frac{\cos\theta_{in} - \cos\theta_{ex}}{\cos\theta_{in}} = 1 - \frac{\cos\theta_{ex}}{\cos\theta_{in}} \tag{7}$$

where θ_{in} and θ_{ex} is the contact angle (°) between mercury and pore wall for intrusion and extrusion. During the MIP test, as the intrusion phase reached its end the applied pressure attained its maximum value P_{max} (MPa). While the extrusion phase began, the applied pressure dropped but the mercury volume did not change instantaneously, i.e. the mercury begins to flow out only at a certain pressure drop ΔP (MPa). If this pressure drop was only attributed to the contact angle hysteresis, the factor α_θ can be evaluated through Equation (7) as the following:

$$d = -\frac{4\gamma\cos\theta_{in}}{P_{max}} = -\frac{4\gamma\cos\theta_{ex}}{P_{max} - \Delta P} , \quad \alpha_\theta = \frac{\Delta P}{P_{max}} \tag{8}$$

where d is the pore diameter (nm), γ is the surface tension of mercury (0.485 N/m).

The maximum pressure corresponds to the smallest pores, but the extrusion process can be

affected by other types of pores, such as the "ink-bottle" pores. It can cause the shift of hysteresis factor, which is considered as an overall property for the pore structure. For the same pore size, the intrusion pressure and extrusion pressure can be described as the following:

$$P_{in} = -\frac{4\gamma\cos\theta_{in}}{d}, \quad P_{ex} = -\frac{4\gamma\cos\theta_{ex}}{d} = -\frac{4\gamma\cos\theta_{in}}{(1-\alpha_\theta)d} \tag{9}$$

where P_{in} and P_{ex} is the intrusion pressure and extrusion pressure (MPa).

Thus, the intrusion curve and extrusion curve can all be expressed in terms of one unique variable, $d/\cos\theta_{in}$, and the pore entrapment volume can be expressed as,

$$v_{en}(\frac{d_i}{\cos\theta_{in}}) = v_{in}(\frac{d}{\cos\theta_{in}}) - v_{ex}(\frac{d}{\cos\theta_{in}})|_{d=d_i} \tag{10}$$

where v_{en} means pore entrapment, v_{in} and v_{ex} means mercury intrusion and extrusion.

To facilitate the discussion, the pore entrapped volume is noted in terms of its fraction instead of absolute value. The pore entrapment fraction, α_{en}, for a specific pore size, d, is defined as the ratio between the pore entrapment volume and the total intrusion volume:

$$\alpha_{en}(\frac{d}{\cos\theta_{in}}) = v_{en}(\frac{d}{\cos\theta_{in}})/v_{in}^{total} \tag{11}$$

In this study, it is assumed that a specific value for intrusion contact angle, θ_{ex}, is 130° and the total fraction of pore entrapment is plotted in **Figure 6**. As can be seen, the entrapment fraction of PC is lower than that of AAS control group, suggesting a lower pore connectivity of AAS than PC and further the entrapment fraction of AAS increased after using CaSt. This means that CaSt could reduce the pore connectivity of AAS. These observations are consistent with the results obtained from the electrical response-based pore connectivity. The results from electrical responses and MIP measurements suggest that the CaSt can improve the pore structure of AAS through pore size distribution and decrease the pore connectivity, both assisting in improving its resistance against water ingress.

3.4.2 Defects in microstructure of AAS

In order to directly assess the influence of CaSt on the pore features of AAS, SEM tests were carried out and the results are shown in **Figure 7**. As highlighted in the red line mark (**Figure 7-(a)**), numerous of defects in microstructure, e.g. microcracks, can be found in the AAS control specimen and the AAS with CaSt showed much less defects, in which more uniform hydration products can be found. More specifically, both width and length of microcracks were dramatically reduced, and most pores are not connected. Yu [65] pointed out that CaSt can reduce C-(A)-S-H cohesion and gels in the hydration products arranged in an order form that may also assist in reducing internal defects in AAS.

Furthermore, CaSt mainly distributed on two locations in AAS mix. One is the holes shown by the circular line in the **Figure 7-(b)** and results obtained from the SEM-EDS suggest that there were CaSt particles at the center. The other is the pores outlined by the square line in **Figure 7-(b)**, which a large amount of CaSt were found around its wall. This is much clear in **Figure 7-(d)** and –**(e)**. In addition, comparing the AAS mix with 4% CaSt (**Figure 7-(b)**) and the one with 8% CaSt (**Figure 7-(c)**), no significant difference is detected, suggesting that a suitable dosage of CaSt is 4%.

3.4.3 Formation of water-repellent film on the pore surface

Due to its hydrophobic alkyl chain, CaSt shows a strong hydrophobicity and can form water-repellent film on the surface of hydration products, which is helpful to decrease the water absorption rate of PC specimens [21]. To assess if the water-repellent film was formed on the surface of AAS pores and its influence on the water sorptivity, the contacting behaviour of PC and AAS with/without CaSt were examined and the results are shown in **Figure 8**. Comparing the features of water drop between AAS

and PC, the water drop on the control AAS group almost disappeared, while prominent hemispherical water droplets on the samples of AAS-45-4% and AAS-45-8% can be observed. This demonstrated that use of CaSt gave AAS a strong hydrophobic ability due to the formation of water-repellent film on the pore surface. As highlighted by Miki et al. [66], when CaSt was in a precipitation state, the normally-oriented thin films of the long chain compounds can be achieved, which was also found by SEM shown in **Figure 8-(c)**. Therefore, formation of water repellent film is another working mechanism for CaSt to reduce the sorptivity of AAS.

4. Conclusions

In this study, the effect of CaSt on the compressive strength and water sorptivity of the AAS cement was investigated. In order to explain working mechanisms of CaSt to improve the sorptivity of AAS, electrical responses (e.g. bulk electrical conductivity, pore solution conductivity), pore structure (pore size distribution, pore geometries, total porosity, connected porosity) and sorptivity behaviours were carefully examined. According to the results obtained, the following questions can be drawn:

1) The use of CaSt can significantly decrease the water absorption rate of AAS and the corresponding sorptivity value is even less than the PC specimen with a similar W/B. Furthermore, the results suggest that the suitable dosage of CaSt is around 4%, beyond which no significant improvement of water sorptivity can be obtained.

2) According to the results, the improvement mechanisms of CaSt can be summarised two main reasons. The first one is optimisation of pore structure of AAS, which include decreases the pore connectivity, introduction of isolated pores, reduction of defects in microstructure and changes of pore size distribution. On the other hand, a water-repellent film was formed on the surface of pores in AAS, when CaSt was added, which could be strongly resist the water ingress into AAS.

3) One issue needs special attention on using CaSt in AAS. The strength development would be affected and specially, a high strength growth rate may not be obtained. This issue might be solved by numerous approaches, e.g. careful selection of raw materials [57], adjustment of mix proportions [18], addition of nano-materials [67], change of activator usage and type [68].

The ultimate goal of this study is to design and manufacture a more environmentally friendly and sustainable cement, wherein high level of GGBFS can be used to its fullest benefit in practical applications, e.g. high resistance against chemical attacks and chloride ingress. Based on established experience, it is not difficult to design an optimised AAS mix to satisfy the target compressive strength with low sorptivity for a specific application.

However, relative limited experience of using CaSt in AAS was obtained in this study and to accelerate the development of a wide-accepted admixture, extended experiments on examining its effects on other performance parameters, e.g. aging features, carbonation, chloride resistance, are desirable.

Acknowledgement

References

[1] China Concrete and Cement-based Products Association (CCPA), 2017 annual development report of slag

industry, 2018.

[2] W. Hinrichs, I. Odler, Investigation of the hydration of Portland blastfurnace slag cement: hydration kinetics, Advances in Cement Research. 2 (1989) 9-13.

[3] S.D. Wang, K.L. Scrivener, Hydration products of alkali activated slag cement, Cement and Concrete Research. 25 (1995) 561-571.

[4] F. Puertas, S. Martınez-Ramırez, S. Alonso, et al., Alkali-activated fly ash or slag cement strength behaviour and hydration products, Cement and Concrete Research. 30 (2000) 1625-1632.

[5] T. Bakharev, J.G. Sanjayan, Y-B Cheng, Resistance of alkali-activated slag concrete to acid attack, Cement and Concrete Research. 33 (2003) 1607-1611.

[6] T Bakharev, J.G. Sanjayan, Y-B Cheng, Sulfate attack on alkali-activated slag concrete, Cement and Concrete Research. 32 (2002) 211-216.

[7] I. Ismail, S.A. Bernal, J.L. Provis, et al., Influence of fly ash on the water and chloride permeability of alkali-activated slag mortars and concretes, Construction and Building Materials. 48 (2013) 1187-1201.

[8] S.A. Bernal, R. Mejía de Gutiérrez, A.L. Pedraza, et al., Effect of binder content on the performance of alkali-activated slag concretes, Cement and Concrete Research. 41 (2011) 1-8.

[9] E. Gartner, Industrially interesting approaches to "low-CO_2" cements, Cement and Concrete Research. 34 (2004) 1489-1498.

[10] K. Yang, C.H. Yang, J.J. Zhang, et al., First structural use of site-cast, alkali-activated slag concrete in China, "Proceedings of The Institution of Civil Engineers-Structures and Buildings", 2017, 1-10.

[11] DBJ50/T-205-2014, Technical specification for application of alkali-activated slag concrete, Standardization Administration of the People's Republic of China, Beijing, 2015, 16 pages.

[12] F. Collins, J.G. Sanjayan, Unsaturated capillary flow within alkali activated slag concrete, Journal of Materials in Civil Engineering. 20 (2008) 565-570.

[13] D.W. Law, A.A. Adam, T.K. Molyneaux,et al., Durability assessment of alkali activated slag (AAS) concrete, Materials and Structures. 45 (2012) 1425-1437.

[14] D. Law, I. Patnaikuni, A.A. Adam, et al., Strength, sorptivity and carbonation of geopolymer concrete, "Challenges, opportunities and solution in structural engineering and Construction-Ghafoori", 2010, 563-568.

[15] K. Yang, C.H. Magee, B. Nanukuttan, et al., Establishment of a preconditioning regime for air permeability and sorptivity of alkali-activated slag concrete, Cement and Concrete Composites. 73 (2016) 19-28.

[16] F. Collins, J.G. Sanjayan, Effect of pore size distribution on drying shrinkage of alkali-activated slag concrete, Cement and Concrete Research. 30 (2000) 1401-1406.

[17] A.R. Brough, A. Atkinson, Sodium silicate-based, alkali-activated slag mortars Part I. Strength, hydration and microstructure, Cement and Concrete Research. 32 (2002) 865–879.

[18] M. Balcikanli, E. Ozbay, Optimum design of alkali activated slag concretes for the low oxygen/chloride ion permeability and thermal conductivity, Composites Part B: Engineering. 91 (2016) 243-256.

[19] M. Rostami, K. Behfarnia, The effect of silica fume on durability of alkali activated slag concrete, Construction and Building Materials. 134 (2017) 262-268.

[20] S. Bernal, R. De Gutierrez, S. Delvasto,et al., Performance of an alkali-activated slag concrete reinforced with steel fibers, Construction and Building Materials. 24 (2010) 208-214.

[21] Z. Ge, Concrete admixture [second edition], Beijing: Chemical industry Publishing House, 2015, 187-188. (in Chinese)

[22] T. He, Concrete admixture, Xi'an: Shanxi science and technology Publishing House, 2003, 165-166. (in Chinese)

[23] A. Maryoto, Resistance of concrete with calcium stearate due to chloride attack ttested by accelerated corrosion, Procedia Engineering. 171 (2017) 511-516.

[24] GB-175, Common Portland Cement, Standardization Administration of the People's Republic of China, Beijing, 2007, 16 pages.

[25] GB/T 17671-1999, Method of Testing Cements-Determination of Strength, The State Bureau of Quality and Technical Supervision, Beijing, 1999, 9 pages.

[26] GB/T 208-2014, Text method for determining cment density, Standardization Administration of the People's Republic of China, Beijing, 2014, 6 pages.

[27] ASTM C642, Standard test method for density, absorption, and voids in hardened concrete, in: Annual Book of ASTM Standards, vol. 04.02, American Society for Testing and Materials, Philadelphia, 2002.

[28] X.H. Zhu, C.H. Yang, K. Yang, et al., Characterisation of pore structure development of alkali-activated slag cement during early hydration using electrical responses, Cement and Concrete Composites. 89 (2018) 139-149.

[29] Z. Rusin, P. Świercz, Volumetric strains of cement-based mortars caused by ice formation in terms of frost resistance diagnostics, Bulletin of the Polish Academy of Sciences Technical Sciences. 63 (2015) 35-41.

[30] ASTM C1585-13, Standard Test method for measurement of rate of absorption of water by hydraulic cement concretes, ASTM International, West Conshohocken, PA, 2013.

[31] RELIM: TC-116, Permeability of concrete as a criterion of its durability, Materials and Structures. 32 (1999) 174–179.

[32] BS-EN:13057, Products and systems for the protection and repair of concrete structures-Test methods: Determination of resistance of capillary absorption, BSI, London, 2002, 16 pages.

[33] BS: 1811, Testing concrete-Part 122: Method for determination of water absorption, BIS, London, 1983.

[34]] A. Vollpracht, B. Lothenbach, R. Snellings, et al., The pore solution of blended cements: a review, Materials and Structures. 49 (2016) 3341-3367.

[35] F. Moro, H. Bohni, Ink-bottle effect in mercury intrusion porosimetry of cement-based materials, Journal of Colloid and Interface Science. 246 (2002) 135-149.

[36] X.H. Zhu, C.H. Yang, K. Yang, et al., Effect of graphene oxide on the mechanical properties and the formation of layered double hydroxides (LDHs) in alkali-activated slag cement, Construction and Building Materials. 132 (2017) 290-295.

[37] H.V. Tran, L.D. Tran, H.D. Vu, et al., Facile surface modification of nanoprecipitated calcium carbonate by adsorption of sodium stearate in aqueous solution, Colloids and Surfaces A: Physicochemical and Engineering Aspects. 366 (2010) 95-103.

[38] R. Jiang, P. Zhang, T.J. Zhao, et al., Study on the waterproof and anti-chloride effect of metal soap on concrete, New Building Materials. 37 (2010) 61-64. (in Chinese)

[39] C. Gao, Effect of chemical admixture on shrinkage cracking of concrete, Beijing: China building materials academy, 2004. (in Chinese)

[40] K. Aligizaki, Pore structure of cement-based materials: testing, interpretation and requirements, Britain : Taylor and Francis, 2014.

[41] O.M. Jensen, P.F. Hansen, Water-entrained cement-based materials I. Principles and theoretical background, Cement and Concrete Research. 31 (2001) 647–654.

[42] K. Kendall, A.J. Howard, J.D. Birchall, et al., The relation between porosity, microstructure and strength, and the approach to advanced cement-based materials, Philosophical Transactions of the Royal Soci. 310 (1983) 139-151.

[43] C. Shi, Strength,pore structure and permeability of alkali-activated slag mortars, Cement and Concrete Research. 26 (1996) 1789-1799.

[44] W. Chen, H.J.H. Brouwers, The hydration of slag, part 1: reaction models for alkali-activated slag, Journal of Materials Science. 42 (2006) 428-443.

[45] D. Krizana, B. Zivanovic, Effects of dosage and modulus of water glass on early hydration of alkali-slag cements, Cement and Concrete Research. 32 (2002) 1181-1188.

[46] P. Duxson, J.L. Provis, G.C. Lukey, et al., Understanding the relationship between geopolymer composition, microstructure and mechanical properties, Colloids and Surfaces A: Physicochemical and Engineering Aspects. 269 (2005) 47-58.

[47] S.A. Bernal, R. Mejía de Gutiérrez, J.L. Provis, Engineering and durability properties of concretes based on alkali-activated granulated blast furnace slag/metakaolin blends, Construction and Building Materials. 33 (2012) 99-108.

[48 S.A. Bernal, J.L. Provis, Durability of Alkali- Activated Materials: Progress and Perspectives, Journal of the American Ceramic Society. 97 (2014) 997-1008.

[49] S. Song, D. Sohn, H.M. Jennings, et al., Hydration of alkali-activated ground granulated blast furnace slag, Journal of Materials Science. 35 (2000) 249-257.

[50] F. Rajabipour, J. Weiss, Electrical conductivity of drying cement paste, Materials and Structures. 40 (2007) 1143-1160.

[51] W.J. McCarter, T.M Chrisp, G. Starrs, The early hydration of alkali-activated slag: developments in monitoring techniques, Cement and Concrete Composites. 21(1999) 277-283.

[52] Q.M. Ma, S.V. Nanukuttan, P.A.M. Basheer, et al., Chloride transport and the resulting corrosion of steel bars in alkali activated slag concretes, Materials and Structures. 49 (2016) 3663-3677.

[53] J.L.Provis, I. Ismail, R.J. Myers, Characterising the structure and permeability of alkali-activated binders, "International RILEM Conference on Advances in Construction Materials Through Science and Engineering", 2011, 493-501.

[54] H. Ye, C. Cartwright, F. Rajabipour, et al., Understanding the drying shrinkage performance of alkali-activated slag mortars, Cement and Concrete Composites. 76 (2017) 13-24.

[55] H. Ye, A. Radlińska, Shrinkage mechanisms of alkali-activated slag, Cement and Concrete Research. 88 (2016) 126-135.

[56] D.M. Roy, Alkali-activated cements opportunities and challenges, Cement and Concrete Research. 29 (1999) 249-254.

[57] X.C. Pu, Alkali activated slag cement and concrete, Beijing: Science Press, 2010. (in Chinese)

[58] J. Kaufmann, Pore space analysis of cement-based materials by combined Nitrogen sorption-Wood's metal impregnation and multi-cycle mercury intrusion, Cement and Concrete Composites. 32 (2010) 514-522.

[59] S.P. Rigby, K.J. Edler, The influence of mercury contact angle, surface tension, and retraction mechanism on the interpretation of mercury porosimetry data, Journal of Colloid and Interface Science. 250 (2002) 175-190.

[60] J. Kaufmann, R. Loser, A. Leemann, Analysis of cement-bonded materials by multi-cycle mercury intrusion and nitrogen sorption, Journal of Colloid and Interface Science. 336 (2009) 730-737.

[61] F. Collins, J.G. Sanjayan, Capillary Shape: Influence on water transport within unsaturated alkali activated slag concrete, Journal of Materials in Civil Engineering. 22 (2010) 260-266.

[62] F. Collins, J.G. Sanjayan, Strength and shrinkage properties of alkali-activated slag concrete containing porous coarse aggregate, Cement and Concrete Research. 29 (1999) 607-610.

[63] F. Collins, J.G. Sanjayan, Cracking tendency of alkali-activated slag concrete subjected to restrained shrinkage, Cement and Concrete Research. 30 (2000) 791-798.

[64] Q. Zeng, K.F. Li, T. Fen-Chong, et al., Analysis of pore structure, contact angle and pore entrapment of blended cement pastes from mercury porosimetry data, Cement and Concrete Composites. 34 (2012) 1053-1060.

[65] J.R. Yu, M.C. Cavallaro, A.A. Chan, et al., Protective effect of sodium stearate on the moisture-induced deterioration of hygroscopic spray-dried powders, International Journal of Pharmacology. 541 (2018) 11-18.

[66] T. MiKi, K. Inaoka, M. Okada, Molecular orientation in the physical-vapour-deposited thin films of calcium stearate, Japanese Journal of Applied Physics. 24 (1985) 672-674.

[67] K. Behfarnia, M. Rostami, Effects of micro and nanoparticles of SiO_2 on the permeability of alkali activated slag concrete, Construction and Building Materials. 131 (2017) 205-213.

[68] S.D. Wang, K.L. Scrivener, P.L. Pratt, Factors affecting the strength of alkali-activated slag, Cement and Concrete Research. 24 (1994) 1033-1043.

List of symbols

α_θ the contact angle hysteresis, $^{\circ}$;

α_{en} the pore entrapment fraction, %;

β the connectivity factor (inverse tortuosity);

γ the surface tension of mercury (0.485 N/m);

θ_{ex} the contact angle between mercury and pore wall for extrusion, $^{\circ}$;

θ_{in} the contact angle ($^{\circ}$) between mercury and pore wall for intrusion, $^{\circ}$;

ρ_P the pastes density, g/cm^3;

ρ_w the density of water, g/cm^3;

σ the electrical resistivity , $\Omega \cdot$m;

σ_0 the conductivity of the pore solution, S;

ϕ_{cap} the volume fraction of capillary porosity, %;

ϕ_C the paste capillary porosity, %;

ϕ_T the paste total porosity, %;

a the constant, mm;

d the pore diameter, nm;

i the volume of water absorbed per unit area, mm^3/mm^2;

l the length of the specimen, m;

m_0 the mass of the samples, g;

m_{dry} the mass of samples cooled in a desiccator to a room temperature, g;

m_{imm} the mass of the surface-dried the specimen, g;

m_{sus} the apparent mass in water, g;

t the time elapsed, min;

v the bulk volume of cement paste, cm^3;

v_{en} the pore entrapment volume, mL;

v_{in}^{total} the total intrusion volume, mL;

A the cross-section area of a specimen, m^2;

$M_{40^{\circ}C}^{0}$ the constant mass of samples dried at 40 $^{\circ}$C, g;

M_S the mass of saturated sample, g;

ΔP the pressure drop, MPa;

P_{ex} the extrusion pressure, MPa;

P_{in} the intrusion pressure, MPa;

P_{max} the maximum pressure, MPa;

R the resistance of a uniform specimen, Ω;

S the sorptivity, mm/min$^{0.5}$;

V their volume determined using a Le Chatelier Flask, mL.

List of Tables and Figures

Table 1 Chemical composition of GGBFS and PC (by mass %)
Table 2 AAS and PC mixture proportions (per liter)
Table 3 Total porosity of samples at the age of 28 day
Table 4 Pore distribution of PC and AAS at the age of 28 day

Figure 1 Effect of CaSt on compressive strength of PC and AAS specimens at different ages
Figure 2 Connected porosity of PC and AAS with/without CaSt at different ages
Figure 3 Water sorptivity of PC and AAS with/without CaSt at the age of 28 days
Figure 4 Summary of electrical responses of PC and AAS and the estimated pore connectivity
Figure 5 Cumulative pore volume (a) and Incremental pore volume (b) of AAS with/without CaSt at 28 days
Figure 6 Total fraction of pore entrapment for AAS samples with different CaSt content
Figure 7 Influence of CaSt on microstructure characteristics of AAS
Figure 8 The action of water-repellent film in the AAS system

Table 1 Chemical composition of GGBFS and PC (by mass %)

Binder	SiO_2	Al_2O_3	Fe_2O_3	MgO	CaO	Na_2O	K_2O	SO_3	LOI
GGBFS	32.12	13.65	1.36	9.15	36.47	0.35	0.47	0.26	0.57
PC	22.54	5.47	2.64	2.74	62.10	0.61	0.18	0.57	3.14

Table2 AAS and PC mixture proportions (per liter)

Parameters	PC-35	AAS-35-0%	AAS-35-4%	AAS-35-8%	PC-45	AAS-45-0%	AAS-45-4%	AAS-45-8%
W/B	0.35	0.35	0.35	0.35	0.45	0.45	0.45	0.45
NaOH pellets (g)	--	20.4	20.4	20.4	--	20.4	20.4	20.4
Sodium silicate (g)	--	184.6	184.6	184.6	--	184.6	184.6	184.6
Water (g)	315	250.1	250.1	250.1	405	346.1	346.1	346.1
n = (SiO_2/Na_2O)	--	1.5	1.5	1.5	--	1.5	1.5	1.5
Cement (g)	900	--	--	--	900	--	--	--
Slag (g)	--	900	900	900	--	900	900	900
CaSt(g)	--	0	36	72	--	0	36	72
Initial porosity(%)	52.4	58.0	55.4	53.1	58.6	63.2	60.8	58.5

Note: PC refers to Portland cement; AAS refers to Alkali-activated slag; 35 and 45 refers to the W/B ratio; 0%, 4% and 8% refers to the dosage of CaSt in AAS mixes.

Table 3 Total porosity of samples at the age of 28 day

Sample	Total porosity (%)	
	W/B=0.35	W/B=0.45
PC	26.3	29.8
AAS-0%	24.0	34.7
AAS-4%	31.1	40.8
AAS-8%	33.9	42.9

Table 4 Pore distribution of PC and AAS at the age of 28 day

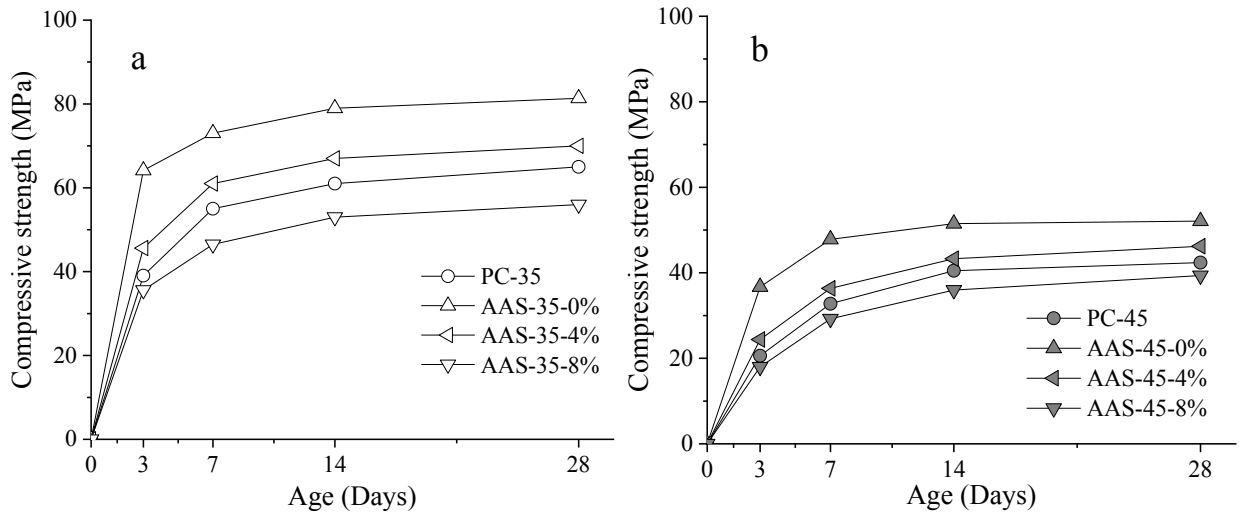| Sample	Volume fraction (%)			
	<10 nm	10-20 nm	20-95 nm	>95 nm
PC-45	19.0	13.3	45.3	22.4
AAS-45-0%	59.6	31.3	4.5	4.6
AAS-45-4%	41.9	44.8	4.7	8.6
AAS-45-8%	36.8	49.2	7.3	6.7

Figure 1 Effect of CaSt on compressive strength of PC and AAS specimens at different ages
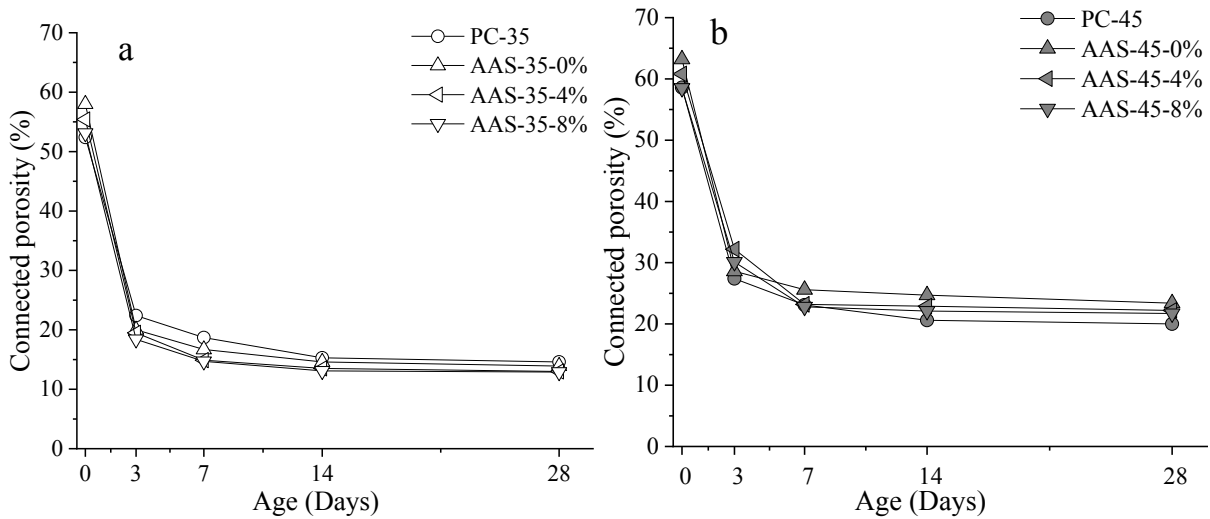(a) W/B=0.35 (b) W/B=0.45

Figure 2 Connected porosity of PC and AAS with/without CaSt at different ages
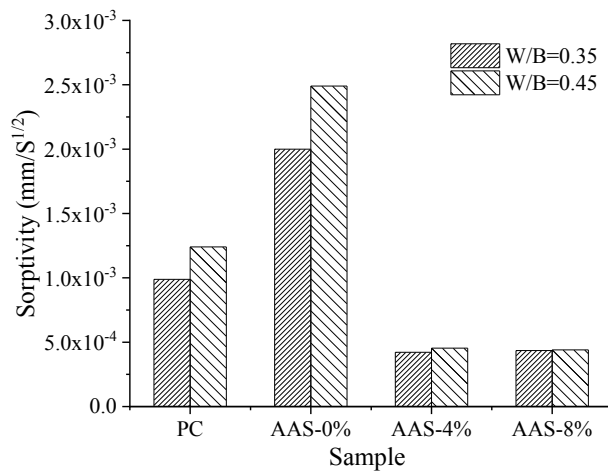(a) W/B=0.35, (b) W/B=0.45

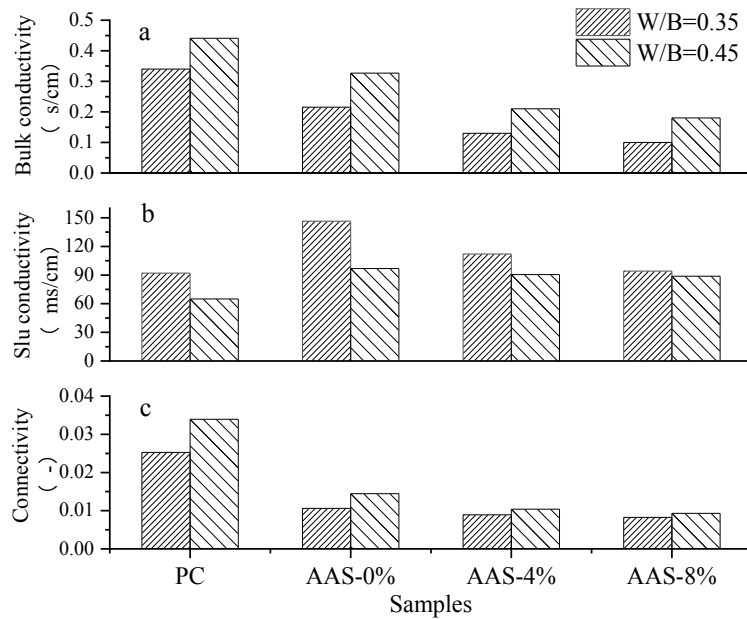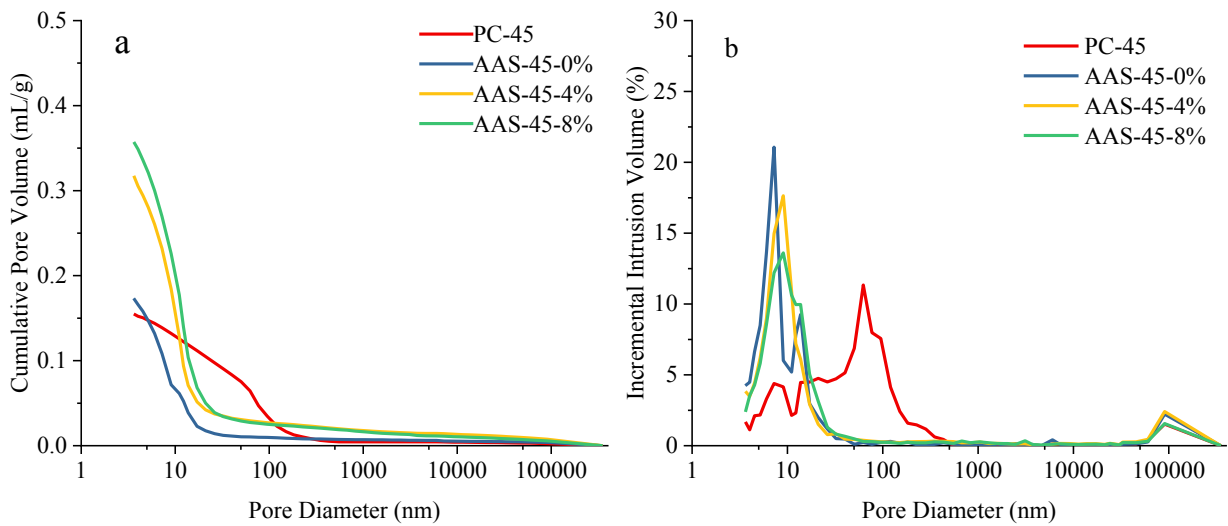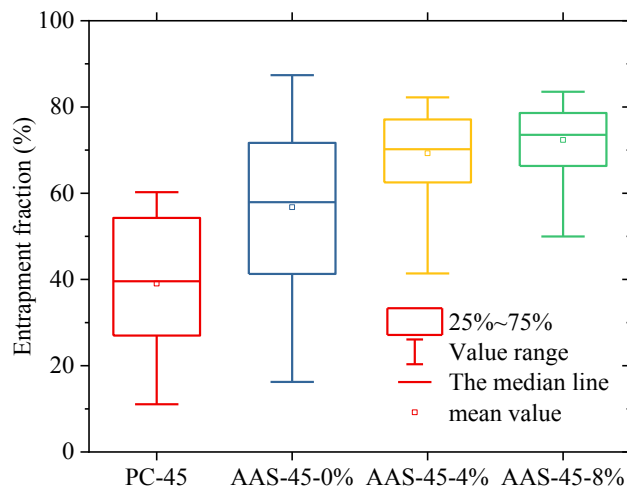**Figure 3** Water sorptivity of PC and AAS with/without CaSt at the age of 28 days

Figure 4 Summary of electrical responses of PC and AAS and the estimated pore connectivity (a) bulk conductivity, (b) pore solution conductivity, (c) connectivity factor

Figure 5 Cumulative pore volume (a) and Incremental pore volume (b) of AAS with/without CaSt at 28 days

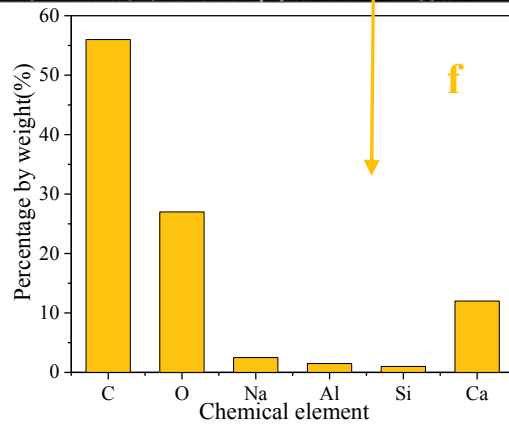**Figure 6** Total fraction of pore entrapment for AAS samples with different CaSt content
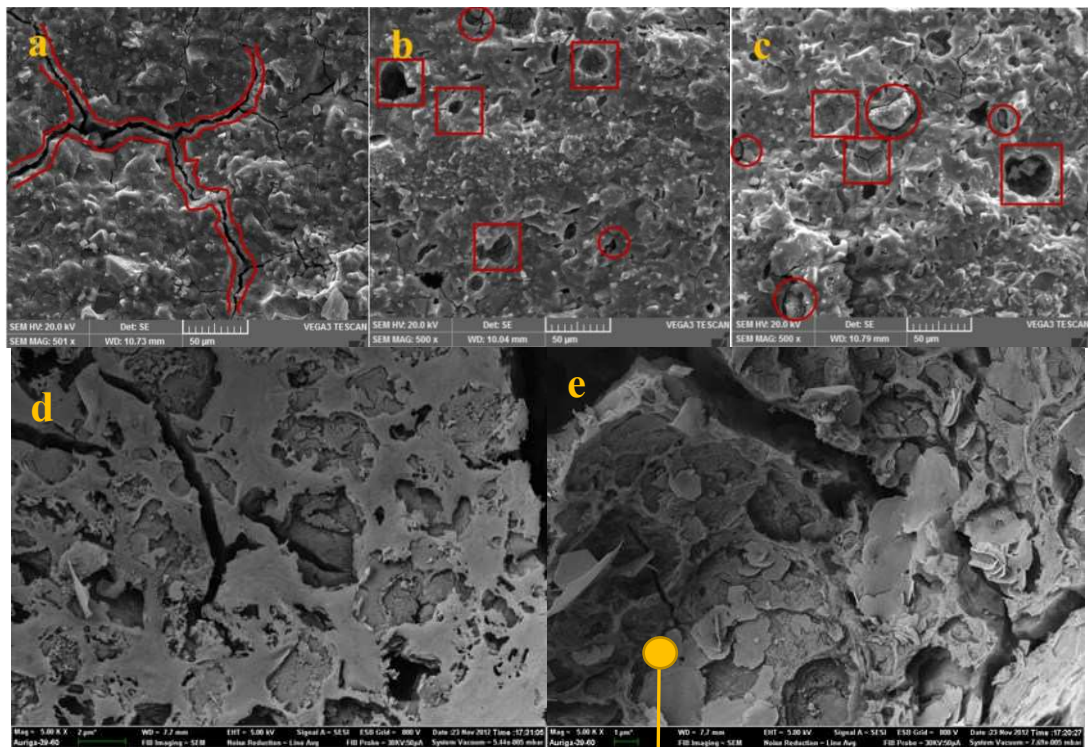
Figure 7 Influence of CaSt on microstructure characteristics of AAS
(a) 45-0% (500X), (b) 45-4% (500X), (c) 45-8% (500X), (d) 45-4% (5000X), (e) 45-8% (5000X), (f) EDS detection of the layered film that formed in AAS pore wall
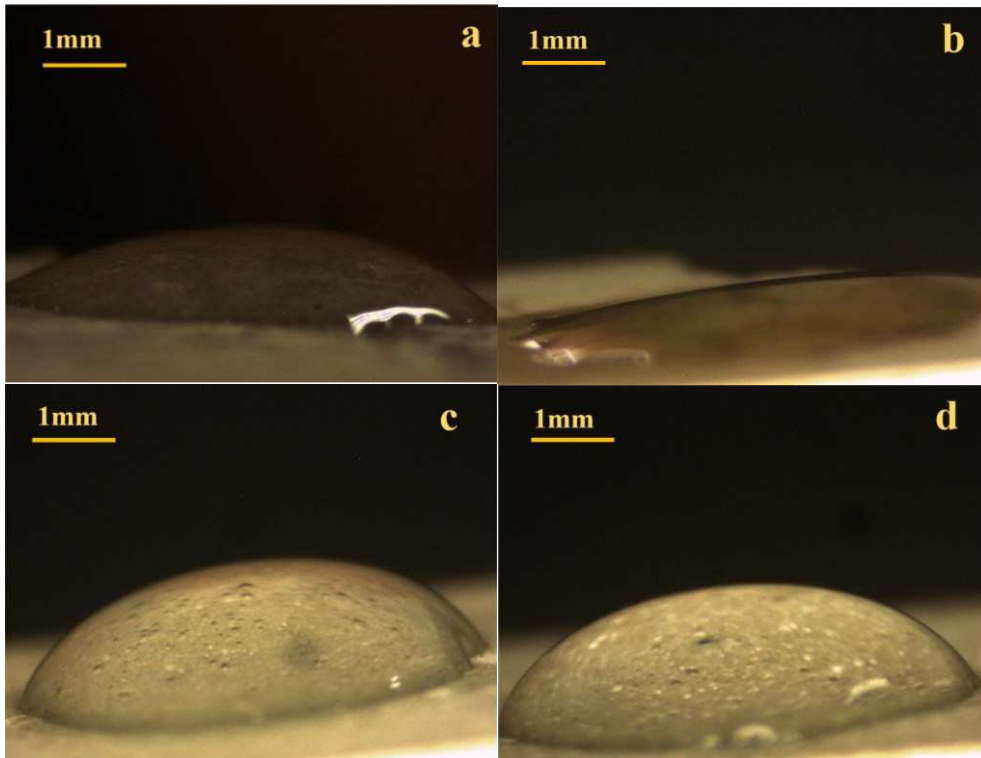
Figure 8 The action of water-repellent film in the AAS system
(a) PC-45, (b) AAS-45-0%, (c) AAS-45-4%, (d) AAS-45-8%